Research on Chemical Intermediates (2019) 45:5781–5800
https://doi.org/10.1007/s11164-019-04002-z

Photogeneration of reactive oxygen species over ultrafine TiO_2 particles functionalized with rutin–ligand induced sensitization and crystallization effects

Przemysław Łabuz, et al. ***[full author details at the end of the article]***

Received: 29 August 2019 / Accepted: 9 September 2019 / Published online: 22 October 2019

Abstract

Interaction of amorphous and crystalline TiO_2 ultrafine particles (2–6 nm) with rutin results in the formation of colored nanomaterials of an excellent dispersity and enhanced colloidal stability in aqueous media. The FTIR and Raman spectra confirmed attachment of the rutin ligand via vicinal hydroxyl groups in a catechol-like fashion. The binding of rutin to amorphous TiO_2 gives rise to spontaneous crystallization of the parent nanoparticles into hydrogen titanates ($H_2Ti_3O_7$ and $H_2Ti_{12}O_{25}$). Such structural transformations result in photosensitization toward visible light with enhanced efficiency of the charge separation and interfacial charge transfer processes, confirmed by detailed photoelectrochemical studies of the examined nanomaterials. The effectiveness of the photocatalytic ROS generation reactions was also strongly influenced by hydrogen peroxide, which plays a double role of a reactant prone to reduction and generation of hydroxyl radicals or a redox agent destroying the intra-band gap electronic states, suppressing thereby charge recombination. The photoinduced charge transfer processes lead to generation of various reactive oxygen species, which were detected by EPR using DMPO spin trap ($HOO^{\cdot}$ detection) and in the reaction with terephthalic acid acting as a chemical scavenger ($HO^{\cdot}$ detection). Complexation of TiO_2 particles with rutin shifts the photogeneration of hydroperoxyl ($HOO^{\cdot}$) and hydroxyl ($HO^{\cdot}$) radicals toward visible light ($\lambda > 400$ nm). A triple effect of rutin attachment to titania was established. It consists in pronounced photosensitization, promotion of crystallization and enhancement of the colloidal stability of ultrafine titania particles. Environmental implications of these assets on the photoinduced redox reactions with hydrogen peroxide in aqueous solutions upon UV or visible light irradiation were also discussed.

Keywords Titania · Complexation · Biomolecules · Sensitization · Radicals · H_2O_2 · Colloidal stability · Environmental (photo)toxicity

Dedicated to the late Professor Michel Che.

Introduction

Transition metal oxide semiconductors, such as titania [1, 2], are promising materials for wide ranging applications as photo-electro-catalysts [3–5], energy conversion materials [6], environmental clean-up agents [7, 8], food additives [9] components of biomaterials [10] and advanced products of pharmaceutical [11], cosmetic [12] or medical relevance [13, 14]. However, incorporation of oxide nanoparticles into such materials may lead to their subsequent uncontrollable release into the environment, in particular into the marine and freshwater systems, and subsequent undesired transfer into the trophic chains. For these reasons, nanoparticles are reported to be of a special concern as potential environmental health hazard agents [15].

Surface of titanium oxide may be functionalized by appropriate coating with organic molecules and therefore tailored for specific applications [16]. Indeed, binding of organic ligands changes dramatically optical, photochemical and photobiological characteristics of the resultant hybrid materials. In particular, TiO_2 may be sensitized to visible light upon complexation of benzene derivatives such as catechol, salicylic or phthalic acids [17, 18]. The ligand –COOH to –OH ratio, extent of the electronic coupling between the relevant energy levels, and appearance of additional states within the band gap allowing for charge transfer from the organic part to the oxide substrate have been found to be crucial for elucidation of their photocatalytic and phototoxic properties. At the same time, surface complexation by organic molecules affects the hydrodynamic stability of the functionalized titania nanoparticles, shifting the point of zero charge (PZC) values and changing the critical coagulation concentration (CCC). These facts facilitate the nanoparticles dispersion and enhance the range of their colloidal stability in aquatic environments [19].

For many years, bulk titania has generally been regarded as a safe material due to its limited toxicity, chemical inertness and high biocompatibility [20]. However, the effects of short- and long-term exposure of living organisms to the nanoparticulate form of TiO_2, in both bare and chemically functionalized states, are still debated being a sensitive topic of wide ranging nanotoxicological studies [19, 21, 22]. Recently, the Scientific Committee on Consumer Safety (SCCS) has described the genotoxic, carcinogenic and photosensitization behavior of TiO_2 nanoparticles (SCCS/1516/13). Toxicity of TiO_2 nanoparticles is also a vivid subject of many in vitro and in vivo studies [23, 24]. Some adverse bioeffects of the nanocrystalline TiO_2, observed for model aquatic organism, include concentration and time-dependent inhibition of the growth rate of living beings [25] or decrease in weight of the internal organs [26]. In this context, ultrafine titania nanoparticles (< 10 nm) are particularly hazardous due to their high stability in aquatic and air suspensions along with high transmembrane penetration ability. Furthermore, spontaneous complexation with adventitious biomolecules, present often in aquatic media, may lead to photosensitization of such particles enhancing their bioenvironmental impact.

Under UV irradiation, all titanium dioxide nanoparticles, regardless of their actual polymorphic form (anatase, brookite or rutile), surface state and crystal

size may exhibit significant phototoxic effects due to generation of reactive oxygen species (ROS), such as hydroxyl radicals, $HO^{\cdot}$, superoxide radicals, $^1O_2$, and hydrogen peroxide, H_2O_2 [27]. Among them, the $HO^{\cdot}$ radicals are exceptionally injurious species in biological milieus due to their high chemical reactivity combined with low selectivity.

Hydrogen peroxide (H_2O_2) is a key intermediate in numerous photocatalytic, biological and environmental processes, and at low concentrations, it is ubiquitous in ground waters, freshwaters and marine environments [28]. A pronounce increase in the concentration of hydrogen peroxide is observed in natural waters when exposed to sunlight as a consequence of photochemical transformations of natural organic matter [28]. The elevated level of H_2O_2 in living cells has also been observed in vivo without photoactivation, as a response to a variety of oxidative stress conditions caused, e.g., by the presence of internalized TiO_2 or other oxide nanoparticles. It is responsible for DNA damage and lipid peroxidation [29, 30]. A plausible mechanism for cellular toxicity is usually associated with generation of $HO^{\cdot}$, $O_2^{\cdot-}$ and H_2O_2 in bacterial cells [31].

Among various reactive oxygen species generated by many photoelectrochemical and photocatalytic processes with TiO_2, hydrogen peroxide plays an important role as a versatile redox active molecule [4]. It can be produced in situ in a series of reactions initiated by water oxidation:

$$H_2O + h_{VB} \rightarrow H^+ + HO^{\cdot} \tag{1}$$

$$HO^{\cdot} + HO^{\cdot} \rightarrow H_2O_2 \tag{2}$$

or dioxygen reduction:

$$O_2 + e_{CB} \rightarrow O_2^{\cdot-} \tag{3}$$

$$O_2^{\cdot-} + H^+ \rightarrow HO_2^{\cdot} \tag{4}$$

$$2HO_2^{\cdot} \rightarrow H_2O_2 + O_2 \tag{5}$$

In turn, H_2O_2 may also be readily reduced by electrons photogenerated in the conduction band of the excited titania, contributing to the enhanced formation of the hydroxyl radicals [32]:

$$H_2O_2 + e_{CB}^- \rightarrow HO^{\cdot} + OH^- \tag{6}$$

All those photochemical processes engaging the hydrogen peroxide molecule are ubiquitously accompanied by the photo-redox steps in which other transient reactive oxygen species appear. In the context of an environmental impact, they may be involved in various uncontrolled extrinsic redox processes with the living organisms. In order to reduce uncertainties related to their potential harmful influence, it is necessary not only to develop methods that are able to detect and quantify titania nanoparticles in real environment [33], but also to evaluate their photochemical/phototoxic properties enhanced by complexation of adventitious biomolecules with –OH/–OOH anchoring functionalities.

In this study, we present the results of sensitization and spontaneous crystallization of ultra-small TiO_2 particles (2–6 nm) upon ligation of molecules of natural

origin, such as rutin [34], for visible light activity and ROS generation efficiency in aquatic media. Photocurrent measurements and experiments using radical scavengers were carried out to elucidate the nature of the photogenerated ROS species, and to evaluate the sensitization efficiency.

Experimental

Synthesis

Two types of ultra-dispersed commercially available titania specimens (*Plasmachem*), differing in size, were functionalized with rutin molecules. A specimen with a particle size of 2–4 nm, labeled hereafter as "A-2" (PL-TiO-N-20p lot), and a specimen with a particle size of 4–6 nm, labeled as "A-6" (PL-TiO-20p lot) throughout this study were used. Surface modification occurred spontaneously upon mixing a colloidal solution of the TiO_2 particles with an aqueous solution containing the organic compound with the initial molar ratio of rutin to TiO_2 equal to 1:1. Directly after the mixing, a color change occurred spontaneously without any precipitate formation. The solution was then placed in a dialysis tube (Sigma, cutoff 14 kDa) and dialyzed against water in order to remove the unbound organic part and any excess of soluble salts.

Characterization

The phase composition and the particle size of the synthesized materials were studied by the powder X-ray diffraction (XRD) techniques, using a Rigaku MiniFlex 600 X-ray diffractometer (Cu Kα radiation, 0.3 mm filter). The registration speed of 3° min^{-1} with the 0.05° steps in the 2θ degree range from 10° to 70° was used. To evaluate the morphology of titania nanoparticles, transmission electron microscopy measurements were carried out using a Tecnai Osiris instrument (FEI) with a X-FEG Schottky field emitter operated at the acceleration voltage of 200 kV. The samples were dispersed in ethanol, ultrasonicated, dropped into a lacey carbon-coated copper grid and then dried at a room temperature. Continuous wave EPR spectra were recorded with an X-band Bruker ELEXSYS-II E580 spectrometer with the 0.1–0.5 mT modulation amplitude. The micro-Raman spectra were recorded at ambient conditions using a Renishaw InVia spectrometer equipped with a Leica DMLM confocal microscope and a CCD detector, using the excitation wavelength of 785 nm. The laser power at the sample position was 1.5 mW. The Raman scattered light was collected in the spectral range of 100–2000 cm^{-1}. FTIR spectra were recorded with a Nicolet 6700 (Thermo Scientific) spectrophotometer, using a single-reflection ATR device with the diamond crystal. UV–Vis absorption spectra of the colloidal solutions were recorded in the range of 250–600 nm by means of a HP 8453 spectrophotometer.

Colloidal stability

Colloidal stability of the titania nanoparticles as the function of salt addition was assessed by mixing water suspension of the TiO_2 nanoparticles with the NaCl solution of different concentrations (from 0 to 0.8 mol dm^{-3}) in a 96-well plate. The final volume was set to 250 µl, and the concentration of the nanoparticles was equal to 0.1 g dm^{-3}. The resultant optical density at 600 nm (OD_{600}) was measured using a Tecan Infinite M200 plate reader and compared with the reference samples without NaCl. The results were presented as a function of increase in the OD_{600} (ΔOD_{600}) values versus the NaCl concentration.

Photoelectrochemical measurements

Photocurrent measurements were performed using an electrochemical analyzer, and a 150-W xenon lamp (XBO-150) was equipped with an automatically controlled monochromator as the light source (Instytut Fotonowy). The measurements were conducted in the three-electrode setup using a platinum wire, and Ag/AgCl (3.0 mol dm^{-3} KCl) as a counter and a reference electrode, respectively. The working electrode—a thin layer of the examined sample—was prepared at the surface of a ITO-coated transparent foil (60 Ω/sq resistance, Sigma-Aldrich). The electrolyte (0.1 mol dm^{-3} KNO_3, pH 6.1) was purged with argon or oxygen for 20 min prior to and during the photocurrent measurement. The working electrodes were irradiated in the range of 330–600 nm through the ITO layer in order to minimize the influence of the film thickness on the measured photocurrents. The influence of hydrogen peroxide on the photocurrent and ROS generation processes was studied by addition of 10 mM H_2O_2 to the electrolyte purged with argon.

Photocatalytic activity

The photocatalytic ROS activity of the samples was tested in the reaction of the terephthalic acid (TA) hydroxylation. The reaction can be monitored by emission spectroscopy as the resultant hydroxyterephthalic acid (TAOH) shows a broad emission band at $\lambda_{max} = 425$ nm when excited at $\lambda_{exc} = 315$ nm. The bare TiO_2 nanoparticles or TiO_2 modified with rutin (0.1 g dm^{-3}) were suspended in 4 cm^3 of the terephthalic acid solution (0.003 mol dm^{-3} dissolved in 0.01 mol dm^{-3} citrate, pH 7) and irradiated with an XBO-150 xenon lamp (Instytut Fotonowy). Total photoactivity of the synthetized nanomaterials was studied using a 320-nm cutoff filter. To extract a visible light part of the photoactivity, a 400-nm cutoff filter (Edmund Optics) was also used. In both cases, the NIR and IR filters (10 cm optical path, 0.1 mol dm^{-3} solution of $CuSO_4$), and heat absorbing glass KG-5 (Edmund Optics) were applied for preventing heating of the sample. In order to study the H_2O_2 influence on the hydroxyl radical formation, hydrogen peroxide was added (0.01 mol dm^{-3}) to the reaction mixture. The samples of 0.1 cm^3 volume collected during the irradiation progress were diluted 20 times prior to fluorescence measurements. For ROS detection by the

EPR measurement, the samples were irradiated by UV light (LED λ_{max} 370 nm) or visible light (LED λ_{max} 427 nm with additional cutoff filter $\lambda > 400$ nm) in the presence of DMPO spin traps.

Results and discussion

The phase identity of the samples was established by powder X-ray diffraction and Raman spectroscopy measurements. The diffraction pattern (Fig. 1) reveals that the investigated parent materials are XRD amorphous (A-2 sample, Fig. 1a) and crystalline (A-6 sample, Fig. 1b), respectively.

For the A-6 sample, the 2θ positions of the observed reflections (Fig. 1b) may be indexed within the *I41/amd* space group (ICSD 653280) of anatase: 25.25 (101), 37.65 (004), 47.95 (200), 54.95 (105), 63.25 (204). There are also few weak peaks that are compatible with a residual monoclinic form of titania ($P2_1/c$), with the (hkl) indexes marked in green. The estimated size of the titania crystallites using the Scherrer equation was equal to 4 ± 1 nm. After interaction with rutin, the XRD pattern of A-6 remained essentially the same, while in the case of the A-2 sample, dramatic changes were observed (Fig. $1a_1$). A quite well-structured pattern that appeared implies crystallization of the initially amorphous titania particles upon mere complexation with rutin (Fig. $1a_1$). The resultant powder diffractogram can be interpreted as a mixture of hydrogen titanates. The green and gray (hkl) indexes mark major reflections for identified $H_2Ti_3O_7$ (C2/m) [35] and $H_2Ti_{12}O_{25}$ (C2/m) [36] phases, respectively. The positions of the reflexes assigned to the {200} planes of $H_2Ti_3O_7$ and the {003} planes of $H_2Ti_{12}O_{25}$ are slightly shifted toward lower 2θ values. The crystal structure analysis revealed that both the families of planes, the {200} and {300} ones, cut the corresponding structures through the hydrogen bonds formed between the successive fragments of both the hydrogen titanates. Thus, the observed shifts of the 2θ values indicate slight expansion of the space between the

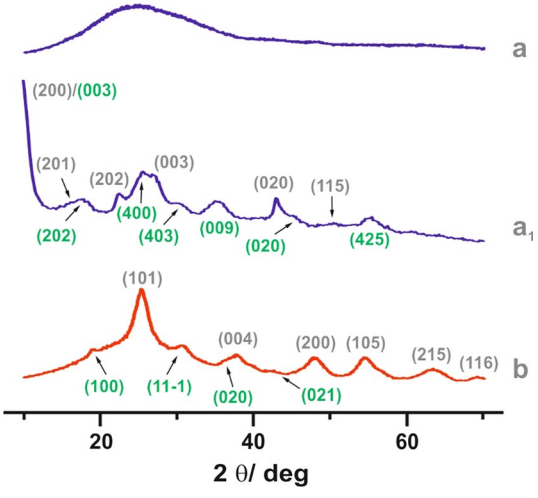

Fig. 1 XRD patterns of the A-2 sample (a), A-2r sample (a_1) and A-6 sample (b). The main diffraction peaks of A-2r correspond to mixture of hydrogen titanate phases (mainly $H_2Ti_3O_7$ with (hkl) indexes marked in gray and $H_2Ti_{12}O_{25}$ with (hkl) indexes marked in green), whereas these of A6 correspond to the anatase structure (Fig. 1b) with spurious contribution of a monoclinic type titania (indexes marked in green). (Color figure online)

stacked layer fragments of $H_2Ti_3O_7$ and $H_2Ti_{12}O_{25}$ produced from the amorphous A-2 sample upon the complexation of rutin.

The composition of the parent and modified titania samples was also examined by Raman spectroscopy, and the results are shown in Fig. 2.

The Raman spectrum of the parent A-2 sample (Fig. 2a) is quite complex, and two groups of lines (100–500 cm^{-1} and 600–1000 cm^{-1}) together with a separate peak at 1450 cm^{-1} can be distinguished. A comparison with the reference spectra of pure anatase, rutile and brookite shows that this spectrum cannot be assigned to a mixture of such polymorphs (though some peaks attributable to those phases appear in the vicinities of the observed RS lines, owing to the common TiO_2 derived origin of the structural motives). The observed bands (115, 187, 270, 380, 442, 663, 752, 835, 903, 947 and 1453 cm^{-1}) are moderately narrow, indicating that some short-range structural order exists in this XRD amorphous sample (see Fig. 1a). This spectrum exhibits some similarity to those observed previously for hydrogenated titania nanosheets/nanoribbons [37, 38], but the group of the peaks in the range 600–1000 cm^{-1} suggests that rather different structures are involved herein. According to the previous studies, the bands in the regions 450–470 and 680 cm^{-1} may be assigned to the distorted TiO_6 octahedra [39]. The framework Ti–O–Ti vibrations are recorded at around 270, 450 and 700 cm^{-1}, whereas the bands around 770, 830–930 cm^{-1} are assigned to Ti–O–H symmetrical stretching modes and Ti–O vibrations observed in various titanate structures [40]. Generally, the bands in the 500–1000 cm^{-1} region are mostly connected to Ti–O–Ti stretching vibrations, and

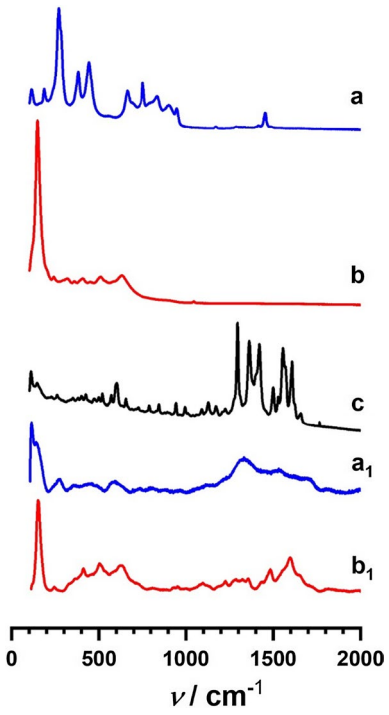

Fig. 2 Raman spectra of the bare titania A-2 (a) and A-6 (b) samples and bare rutin reference (c), together with the corresponding spectra of the rutin modified A-2r (a_1) and A-6r (b_1) materials

their variety can be ascribed to differences in the Ti–O bond lengths [39]. As a result, the Raman features of the A-2 sample may roughly be regarded as a reflection of various six-coordinated titanium–oxygen structures of different local configurations that are randomly organized in space forming the XRD amorphous material. A more detailed assignment of such complex Raman spectra requires a separate study, which is beyond of the intended context of this work. In contrast, the Raman lines observed for the titania A-6 sample are fully consistent with the anatase tetragonal structure, D_{4h}^{19}, and arise from the $A_{1g}+2B_{1g}+3E_g$ active modes (Fig. 2b). The three peaks at 143, 196 and 639 cm^{-1} are assigned to the E_g vibrations and the peak at 397 cm^{-1} to the B_{1g} vibrations. The peak at 516 cm^{-1} is a doublet of the A_{1g} and B_{1g} modes. The measured Raman spectrum shows that the anatase grains are fairly crystalline in a good agreement with the XRD results (see Fig. 1b).

The Raman spectra of the A-2r and A-6r samples are shown in Fig. 2a_1 and b_1, whereas the reference spectrum of rutin is shown in Fig. 2c. As it can be inferred from Fig. 2a_1, complexation with rutin leads to dramatic changes in the Raman spectrum of the A-2 sample, similarly to the analogous changes in the corresponding XRD patterns (cf. Figure 1a, a_1). The bands characteristic for scarce randomly distributed titanium–oxygen fragments dominant in the parent amorphous sample vanishes, and new peaks that appeared make the RS spectrum closer to that observed for the A-6r sample (Fig. 2b_1). Such spectrum may be associated with the formation of quite well-structured hydrogen titanates such as $H_2Ti_3O_7$ and $H_2Ti_{12}O_{25}$ [37], in accordance with the XRD measurements (see Fig. 1a_1). The group of bands in the range of 1300–1800 cm^{-1} confirms, in turn, a successful attachment of rutin to the titania particles in both cases, as it can be inferred from comparison with the reference Raman spectrum of the bare rutin. More detailed inspection into the ligation of the rutin molecules can be obtained from analysis of the IR spectra shown in Fig. 3.

Comparison of the infrared spectra of free and surface attached rutin shows that for both the A-2r and A-6r samples, the IR lines become generally broadened, and some of them are also shifted. The functional groups of rutin give rise to absorption bands observed at 3423 cm^{-1} (O–H stretch), 2989 cm^{-1} (C–H stretch), 1656 cm^{-1}

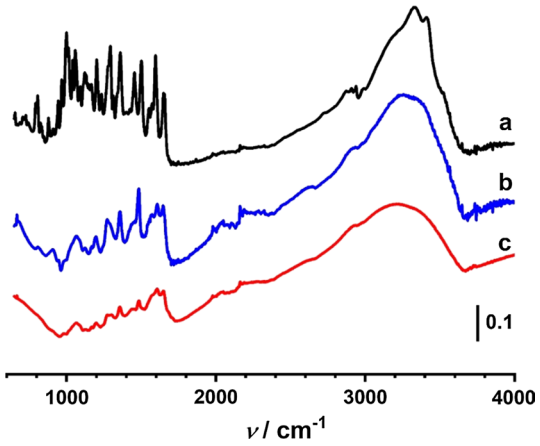

Fig. 3 Infrared spectrum of the parent bare rutin (a), and IR spectra of the A-2r (b) and A-6r (c) samples

(C=O stretch), 1603 cm^{-1} (C=C stretch aromatic ring), 1362 cm^{-1} (O–H bending) and 1296 cm^{-1} (C–O–C). Among these peaks, significant shifts are observed in the hydroxyls oscillation frequencies, which are accompanied by the change in the band shapes. Indeed, the numerous phenyl –OH groups strongly interact with TiO_2 surface, especially when they form vicinal catechol-like arrangements. As a result, the ν(C=C) stretching frequency of the benzene ring skeleton was also shifted from 1596 to 1607 cm^{-1} and from 1502 to 1483 cm^{-1} after forming a complex, due to the enhanced conjugation effect caused by the chelation. The ν(C–O) stretching and the ν(C–O–H) bending vibrations of the dihydroxyphenyl ring (catechol ring) in the range of 1000–1011 cm^{-1} were also substantially decreased. On the other hand, the ν(C=O) stretching oscillation at 1650 cm^{-1} of the heterocyclic ring and the ν(C–O) stretching at 1062 cm^{-1} in the mannopyranosyl rings remain essentially intact, indicating that these functionalities are not involved in the rutin complexation process. These results reveal clearly that rutin molecules are attached via vicinal hydroxyl groups, similarly to epitomic catechol molecules forming quite strong bonds [17]. The released protons are then absorbed by the amorphous titania particles, inducing their transformation into crystalline hydrogen titanates. Owing to the ultrafine dispersion of titania particles (~2–4 nm), the high rutin/TiO_2 ratio is favorable for occurring of such process not only at the surface region (as in the case of larger crystalline A6 particles), but also it allows for an efficient penetration of protons into the bulk of the A-2 grains. As a result, the complexation reaction may be considered as a Bronsted acid–base process, where rutin molecules act as an efficient proton donor ($pK_a = 6.3$) and the amorphous titania nanoparticles as a proton sink.

The structure, size and shape of the A-2r and A-6r particles were next examined by TEM techniques (Fig. 4). As it can be inferred from the obtained image of the A-2r sample (Fig. 4a_1, b_1), rather regular crystalline particles of nearly oblong shape and 2–4 nm size are embedded in a carbonaceous matrix made of the rutin component. The A-6r particles exhibit more rounded shapes of 4–6 nm diameter (Fig. 4c_1), in accordance with the XRD results. They may also form compact aggregates, produced most probably by an oriented attachment. An example of the such double-crystallite grains is shown in Fig. 4d_1.

Figure 4a_1 presents a conventional TEM (CTEM) image of the A-2r sample. The corresponding electron diffraction pattern is presented in Fig. 4a_2. The radius of each detected diffraction rings can be assigned to $H_2Ti_3O_7$ (yellow circles) and $H_2Ti_{12}O_{25}$ (green circles) phases, present simultaneously. Their atomic structures are shown in Fig. 4a_3 and a_4, respectively. In Fig. 4b_1, a high-resolution image of a selected $H_2Ti_3O_7$ nanocrystal is also displayed, along with its indexed diffraction pattern (Fig. 4b_2, b_3), and a properly oriented atomic structure of the $H_2Ti_3O_7$ phase. The lower panel presents an analogous analysis of the A-6r sample. A CTEM image (Fig. 4c_1) together with the associated diffraction pattern (Fig. 4c_2) confirms the anatase structure of the examined titania nanocrystals (Fig. 4c_3). The last panel shows the high-resolution image of a twinned anatase crystallites (Fig. 4d_1). The diffraction pattern analysis approves their anatase nature (Fig. 4d_2, d_3). An accordingly oriented model of the latter structure is presented in Fig. 4d_4. Summarizing, the results obtained from TEM microscopic analysis agree well with both the XRD and RS measurements.

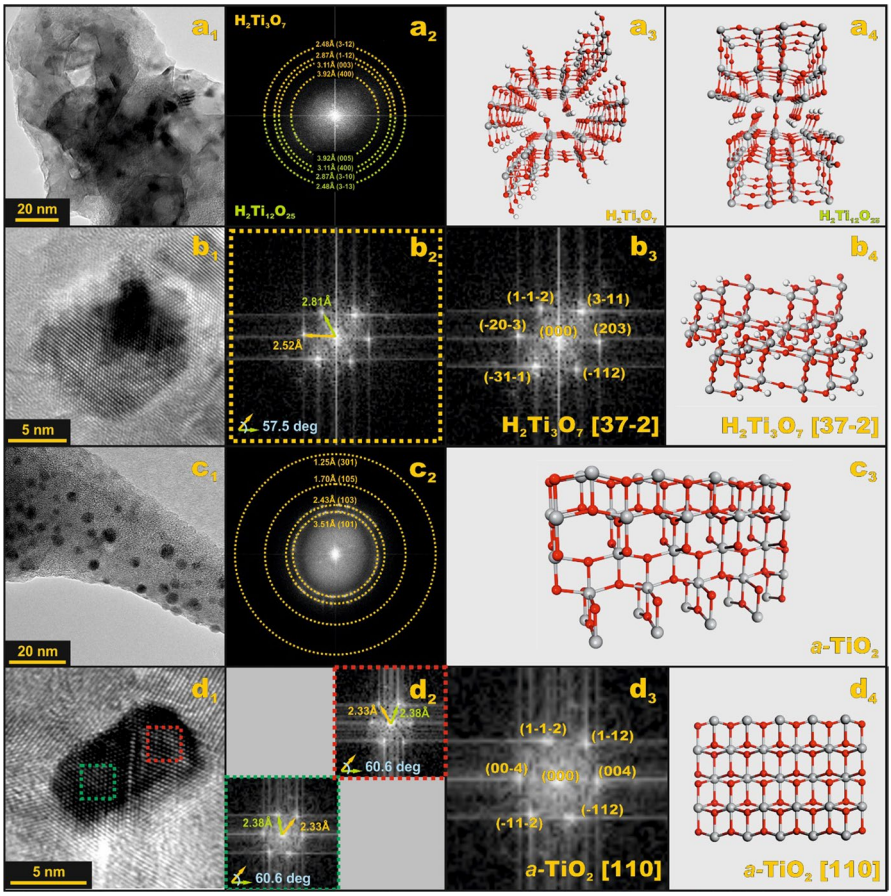

Fig. 4 TEM images of the A-2r ($\mathbf{a}_1$–$\mathbf{b}_4$) and A-6r ($\mathbf{c}_1$–$\mathbf{d}_4$) samples. A CTEM image of the A-2r sample ($\mathbf{a}_1$) together with the corresponding electron diffractogram ($\mathbf{a}_2$) and the assigned structures of the hydrogen titanates ($\mathbf{a}_3$ and $\mathbf{a}_4$). High-resolution image of a $H_2Ti_3O_7$ nanocrystal ($\mathbf{b}_1$) together with the corresponding electron diffractograms ($\mathbf{b}_2$–$\mathbf{b}_3$), and a properly oriented ball and stick structure representation of the $H_2Ti_3O_7$ fragment. CTEM image of the A-6r sample ($\mathbf{c}_1$), along with the corresponding electron diffractograms ($\mathbf{c}_2$), and the assigned anatase structure of the examined titania grain ($\mathbf{c}_3$). High-resolution image of a twinned *a*-TiO_2 nanocrystal ($\mathbf{d}_1$) together with the corresponding electron diffractograms ($\mathbf{d}_2$–$\mathbf{d}_3$), and a properly oriented model of the anatase structure

The agglomeration state of the functionalized A-2r and A-6r nanoparticles in aqueous media was next examined by DLS method, and the results are shown in Fig. 5a. For both colloidal solutions, a clear unimodal distribution of particles is observed, with the sole major peaks located at 2.1 nm and 12.9 nm for the A-2r and A-6r sample, respectively.

The obtained results revealed that A-2r particles when dispersed in water exhibit small tendency to agglomeration, in contrast to the A-6r particles that exist mainly in the form of 3-fourfold clusters.

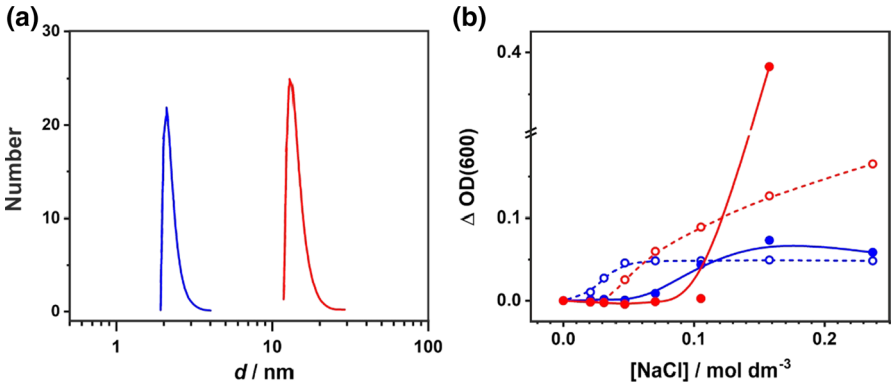

Fig. 5 **a** Particle size distribution for the A-2r (left) and A-6r (right) samples, along with (**b**) variation of the turbidity upon addition of NaCl to the solution (bare A-2 sample—open circles and dashed line, A-2r sample—full circles and solid line, bare A-6—open circle and dashed line, A-6r—full circles and solid line)

The colloid behavior of the suspended nanoparticles exhibited a strong dependency on the ionic strength of the solution. Measurements of the turbidity increase, ΔOD(600), shown in Fig. 5b, imply that the bare A-2 and A-6 nanoparticles form agglomerates within few seconds when NaCl was added to the solution in the concentration as little as 20 mmol dm^{-3} (A-2 sample) and 40 mmol dm^{-3} (A-6 sample). However, modification of the titania grains by rutin protects the particle surface and prevents from precipitation until the concentration of NaCl reaches 70 mmol dm^{-3} (A-2r sample) or even over 110 mmol dm^{-3} for the A-6r sample. The reason for such behavior may be traced back to the high hydrophilic nature of the carbohydrate moiety of the rutin molecule. These results showed also that the attachment of rutin (or other akin biomolecules) extends significantly the range of the colloidal stability of titania ultrafine particles in aquatic media.

Photoelectrochemical account

The characterization results described above revealed that the investigated titania nanomaterials form well-dispersed colloids of high stability with no (A-2) or little light scattering (A-6). Both the rutin modified samples, in turn, form clear orange colloidal solutions, with a negligible level of the light scattering (no signs of turbidity). For all materials, the corresponding UV–Vis absorption spectra are presented in Fig. 6. Generally, the rutin modified colloids exhibit two apparent absorption features. In the UV range, the absorption is characteristic for the titanium dioxide core, as it can easily be inferred from comparison with the reference spectrum of the parent TiO_2.

A second characteristic range of the absorption is located at the border of the UV and visible light and may be assigned to the charge transfer band due to the formation of Ti(IV)-L(rutin) surface complexes. The resulting absorption is extended up to 600 nm with a pronounced maximum located at ~400 nm. Although the rutin

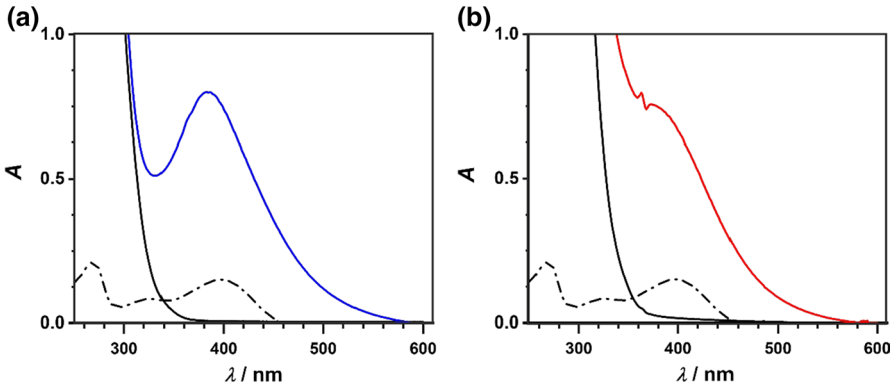

Fig. 6 UV–Vis absorption spectra of colloidal solutions of titania modified with rutin for **a** the A-2r sample and **b** the A-6r sample. The reference spectra of the bare rutin (dotted lines) and the parent TiO_2 (dashed lines) are shown for the sake of comparison

ligand alone absorbs also in this region, there is a substantial increase in the visible light absorption owing to development of the surface charge transfer complexes, which dominates the spectrum. Following our previous studies of TiO_2 modified with catechol, where analogous CT band at 400 nm is formed, we may assign this band to the direct one-step electron injection process via HOMO (rutin) → CB(TiO_2) transitions. Thus, the obtained materials can be classified as the class B photocatalysts [41].

A useful tool to validate photoactivity of the investigated materials is to measure the photocurrent. The intensity of the observed photocurrent versus wavelength may then be used to calculate the efficiency of this process (IPCE—incident photon-to-current efficiency). The obtained IPCE profiles of the bare and surface modified titania deposited on the ITO electrodes at the electrode potential of − 200 mV versus Ag/AgCl are presented in Figs. 7 and 8.

The photoelectrochemical responses of the two bare TiO_2 nanomaterials are different. Whereas the A-6 sample is active within the UV absorption region, giving distinct cathodic photocurrents, the A-2 sample is clearly not active (no reliable action spectrum could be recorded). The IPCE profiles of the surface modified nanomaterials follow the absorption spectra of the examined nanomaterials (Fig. 6). However, there is a substantial difference in the IPCE profiles of both the samples for $\lambda < 360$ nm. A clear IPCE increase is observed at the shortest wavelengths for A-6r sample, whereas negligible values are observed in the case of A-2r one. It is evident that for the rutin modified titania (A-6r), there are two distinct signals originating from the activity of the titania core in the UV range, and from the surface complex at longer wavelengths, due to the charge transfer transitions induced by visible light. In the case of the A-2r sample, the latter transition dominates, while the direct excitation of the A-2 core leads mostly to deactivation processes. This conclusion is supported by the IPCE measurements of the bare A-2 sample, and also by its low photoactivity in EPR and photocatalytic tests (vide infra). Efficient recombination of the photogenerated holes and electrons in

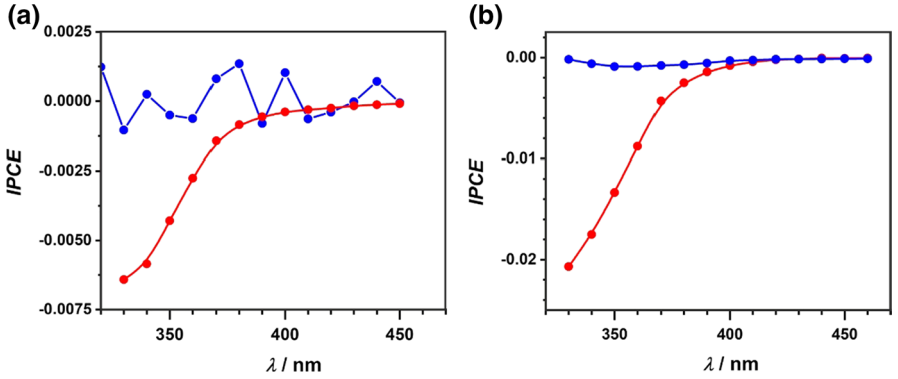

Fig. 7 IPCE profiles of the ITO-working electrodes at − 200 mV (**a**), and IPCE profiles of the ITO-working electrodes covered with the A-2 (blue) or A-6 (red) layer (**b**) in the electrolyte supplemented with H_2O_2 at − 200 mV. (Color figure online)

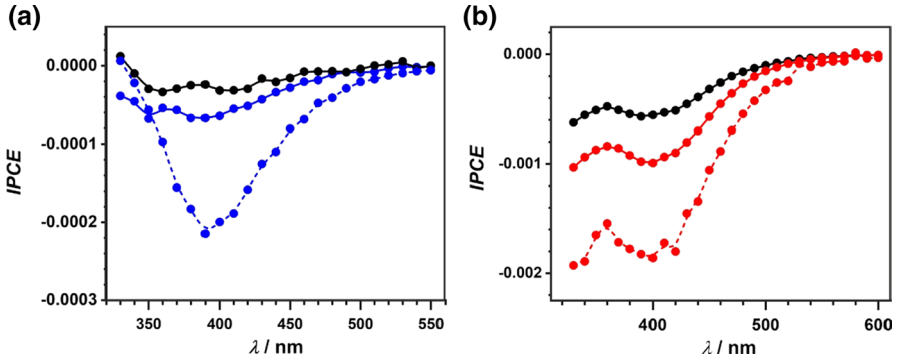

Fig. 8 IPCE profiles of the ITO-working electrodes covered with an A-2r layer (the electrolyte was purged with argon—black or oxygen—blue solid lines), and for the electrolyte supplemented with H_2O_2—blue dashed line (**a**). IPCE profiles of the ITO-working electrodes covered with an A-6r layer (the electrolyte was purged with argon—black or oxygen—red solid lines), and for the electrolyte with H_2O_2 added—red dashed line (**b**). (Color figure online)

the valence and conduction bands results very likely from the amorphous nature of this sample, revealed by XRD. Such materials possess strongly disturbed band structure with numerous intra-bandgap states that facilitate relaxation and charge recombination processes. For the modified materials, the observed IPCE profile is lower than for the bare TiO_2, which may result from an UV filtering effect caused by the organic surface ligand. An alternative explanation may be traced back to the fact that adhesion of the very hydrophilic rutin modified titania to the ITO surface was rather poor, giving rise to less effective contact of the deposited nanomaterials with the ITO electrode. Nonetheless, a substantial extension of the photoactivity toward visible light upon complexation of the titania nanoparticles with rutin was confirmed definitely.

An oxygen sensitive response is evidenced by the pronounced increase in the cathodic photocurrents upon application of the negative potential in the presence of dioxygen. This observation reveals clearly the role of O_2 as an efficient electron acceptor, which is reduced to superoxide radical anion ($E^\circ = -0.18$ V). Such process is known to play a crucial role in the photocatalytic reactions leading to generation of other reactive oxygen species as well [42]. What is important, this phenomenon was observed after the complexation not only within the ultraviolet, but also in the visible range.

The visible light-induced photocurrent generation confirms successful photosensitization of the titania by the rutin complexes, and ligation-induced crystallization of the originally amorphous A-2 titania grains. What is even more important, it proves an effective separation of the photoinduced charges, electrons in the conduction band and holes localized in the oxidized rutin moiety, which is diagnostic for the class B photomaterials. The trapped holes are next involved in the oxidation processes of organic adspecies (including auto-oxidation of rutin) [17], or in the reaction with superoxide leading to formation of singlet oxygen [43]. Addition of H_2O_2 to the electrolyte solution, in turn, enhances significantly the cathodic photocurrents due to the hydrogen peroxide reduction:

$$H_2O_2 + e^- \rightarrow OH^- + HO^{\cdot}$$

opening an alternative channel of the hydroxyl radicals generation (a reductive pathway operating also under visible light).

The nature of the generated ROS ($HO^{\cdot}$ and $HOO^{\cdot}$ species) upon UV and visible light irradiation was examined by EPR spectroscopy using 5,5-dimethyl-1-pyrroline N-oxide (DMPO) as a spin trap, and the obtained results are collated in Fig. 9A and B. In the case of the bare A-2 titania upon illumination either with UV or visible

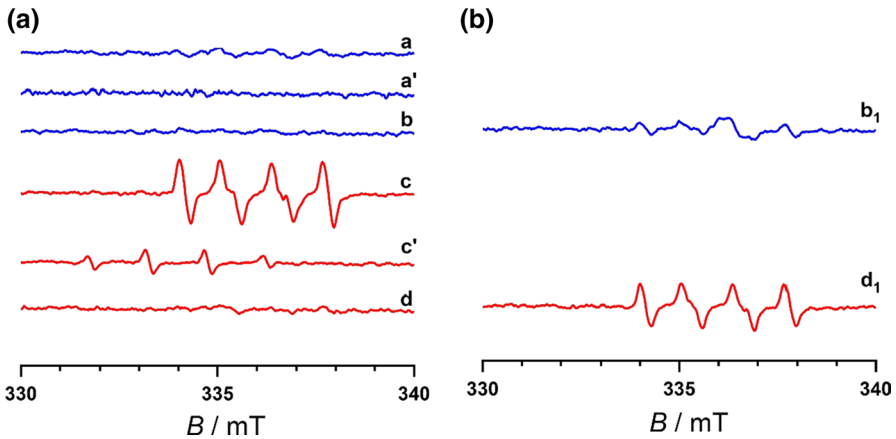

Fig. 9 **A** EPR spectra of DMPO adducts with the photogenerated radicals for bare A-2 (blue) and A-6 (red) samples upon irradiation with UV and visible light. **B** EPR spectra of DMPO adducts with the photogenerated radicals for A-2r (blue) and A-6r (red) samples irradiated with visible light. The spectra a, b, b_1, c, d, d_1 stand for the detection of DMPO-$HOO^{\cdot}$ adducts, whereas a' and c' for detection of the DMPO-$HO^{\cdot}$ adducts. (Color figure online)

light, no EPR signals due to $HOO^{\cdot}$ (Fig. 9a, b) and $HO^{\cdot}$ radicals could be detected (Fig. 9a'). Different photo-behavior was observed for the A-6 sample, where the UV illumination led to appearance of well-resolved EPR signals, diagnostic for generation of the $HOO^{\cdot}$ (Fig. 9c) and $HO^{\cdot}$ (Fig. 9c') radicals. However, under visible light this sample was photo-inactive again (Fig. 9d).

The photo-behavior of the titania particles was significantly changed upon complexation with rutin. Unlike the parent bare titania, both the modified materials exhibit a clear photoactivity in generation of $HOO^{\cdot}$ radicals, with the A-2r sample being less active (Fig. $9b_1$) than the A-6r one (Fig. $9d_1$). Yet, we could not detect the hydroxyl adducts, using this spin trapping technique. Therefore, for monitoring the progress of the hydroxyl radicals formation upon UV–Vis irradiation of the suspended materials, we applied terephthalic acid (TA) as a more efficient scavenger than the DMPO spin traps used in the EPR experiments. The efficiency of the photocatalytic reactions of all the investigated nanomaterials in aqueous solutions was evaluated by monitoring the intensity of the fluorescence peak at 425 nm from the excited ($\lambda_{exc} = 315$ nm) 2-hydroxyterephthalic acid (TAOH), which accumulates during the irradiation progress.

There is a clear difference in the activity between the two bare A-2 and A-6 materials under the applied irradiation conditions ($\lambda > 320$ nm). Only the A-6 specimen was able to produce the hydroxyl radicals when irradiated with the UV light.

The photoactivity of the A-2 nanomaterial was detected only after addition of an electron acceptor (H_2O_2) of a higher reduction potential than dioxygen ($E^{\circ} = 0.81$ V for H_2O_2 vs. -0.18 V for O_2) [44]. Interestingly, in such a case the hydroxyl radical generation productivity upon irradiation with $\lambda > 320$ nm light for the A-2 and A-6 samples is comparable (Fig. 10b), showing that the efficiency of the reductive pathway is higher than the oxidative one. The presence of hydrogen peroxide may also destroy the intra-bandgap states and therefore attenuate the recombination channel. Yet, further studies on the influence of H_2O_2 on the lifetime of photogenerated

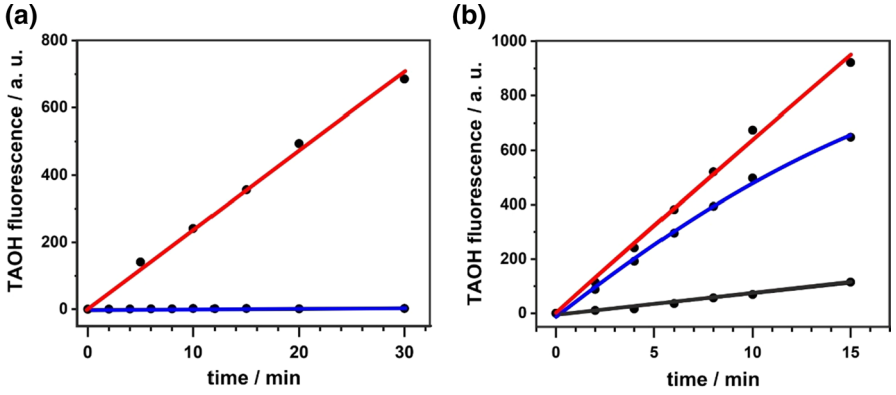

Fig. 10 Increase in the TAOH fluorescence probing the hydroxyl radical generation during the irradiation ($\lambda > 320$ nm) for the A-2 (blue) and A-6 (red) sample in the absence of H_2O_2 (**a**), and in the presence of H_2O_2 (**b**). The black line (**b**) represents the reference intensity of the TAOH fluorescence in the absence of the nanoparticles. (Color figure online)

charges are needed for validation of this hypothesis. It should be, however, emphasized that despite their lower reduction potential dioxygen molecules are also reduced to $HOO^{\cdot}$ radicals, as clearly revealed by the EPR measurements (vide supra) (Fig. 9).

The photocatalytic experiments with the terephthalic acid used as a fluorescent radical scavenger support the results of the photoelectrochemical measurements. For both the TiO_2 materials, modification with rutin leads to a significant hydroxyl radical generation when irradiated with visible light ($\lambda > 400$ nm). The sensitized A-6r samples are substantially more active than the A-2r ones under the visible light (after 15 min of the exposure the amount of the generated TAOH was ca. five times higher). The A-2r nanomaterials are, however, more susceptible to hydrogen peroxide in the solution when compared to A-6r. The photogeneration of the hydroxyl radicals in this case is increased ~ 10 times (Fig. 11). Most probably, it is caused by the better dispersion of A-2r in comparison with A-6r in aqueous suspensions, as revealed by the DLS measurements (see Fig. 5a). This confirms the photoelectrochemical results, which showed that in the visible region, where the absorption due to the charge transfer complex formation is the most efficient, the IPCE profiles are very sensitive to H_2O_2.

Mechanisms and environmental implications

Generation of ROS at the surface of the photoexcited titania is possible through oxidative or reductive pathways (Fig. 12), and the mechanism that operates is essentially dependent on the energy of light that excites the examined photomaterials. In the UV light, both the electron in the conduction band and the hole in the valence band are available; hence, the generation of ROS is efficient and direct oxidation of water is feasible. This mechanism is completely inefficient in the case of the

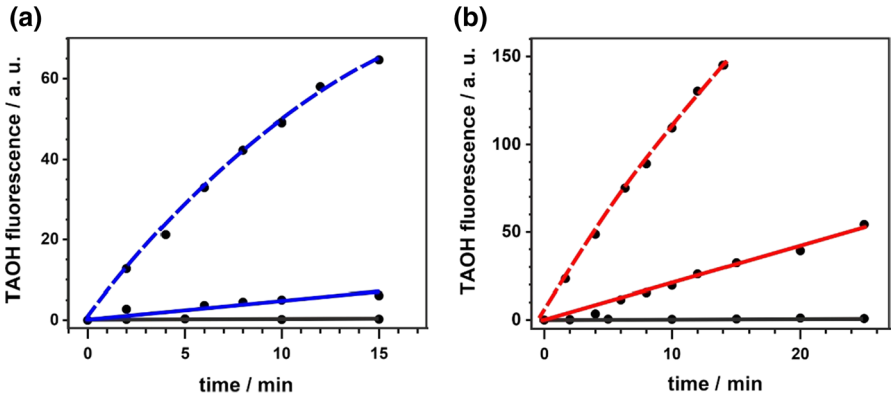

Fig. 11 Increase in the TAOH fluorescence probing the hydroxyl radicals generation during visible light irradiation ($\lambda > 400$ nm) for the A-2r (blue line) sample (**a**), and for the A-6r (red line) sample (**b**). Data collected in the absence of H_2O_2 are represented by solid lines, whereas those measured in the presence of H_2O_2 by dashed lines. The reference black lines represent changes in the intensity of the TAOH fluorescence in the presence of the parent bare TiO_2 nanoparticles. (Color figure online)

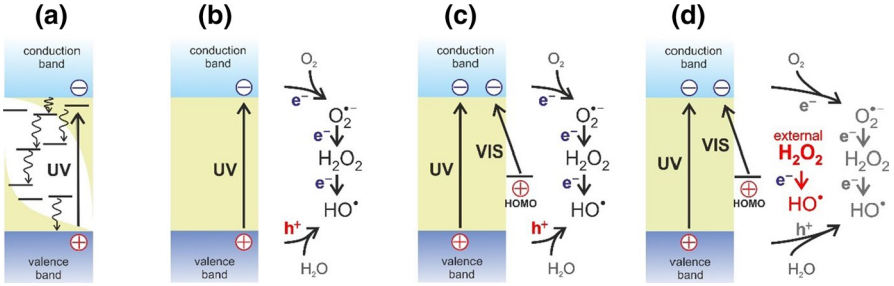

Fig. 12 The mechanism of ROS generation over bare and rutin modified TiO_2 nanomaterials upon irradiation. Photochemically inactive A-2 sample (**a**), UV active A-6 sample (**b**), visible light active A-2r and A-6r samples without H_2O_2 addition (**c**) and in the presence of H_2O_2 (**d**)

amorphous A-2 sample since the abundant intra-bandgap states lead to rapid photochemically unproductive relaxation (Fig. 12a). Yet, for the crystalline A-6 sample of anatase structure, with scarce states in the band gap, it may operate successfully (Fig. 12b). Upon visible light irradiation of the A-2r and A-6r nanomaterials, generation of the hydroxyl radicals is initiated by the reduction of dioxygen to superoxide species by engaging the conduction band electrons (Fig. 12c, d). This triggers the hydroxyl radical production along a pathway involving transfer of three electrons from the conduction band (Fig. 12b, c). The generated (or accidentally encountered in the environment) hydrogen peroxide plays the role of an important intermediate reagent in the photocatalytic process as a reservoir of hydroxyl radicals that may be released upon reduction via an electron donation from the conduction band of the TiO_2 core. Thus, an excess of hydrogen peroxide opens an efficient route for production of copious hydroxyl radicals in a more straightforward one electron process under both the visible and UV light irradiation (Fig. 12d). In addition, deactivation of intra-bandgap electronic states by external H_2O_2, decreasing efficiency of recombination processes is also expected.

The proposed mechanism of ROS generation may have important implications not only for understanding the photocatalytic processes involving H_2O_2 but also for their appearance in biological and environmental systems, where non-Fenton photoactive oxide nanoparticles, such as titania, are present. The obtained results show clearly that the ultrafine titania nanoparticles can efficiently be stabilized in aqueous media upon complexation with large organic molecules containing vicinal –OH groups as efficient anchoring functionalities. Such hybrids are reluctant to coagulation in the presence of salts, implying their possible persistent presence for long period of time, once released to aqueous environments. The organic component acts as an efficient sensitizer giving rise to B-type photocatalytic behavior under visible light irradiation and also as an efficient colloid stabilizing agent. In the case of ultrafine amorphous titania nanoparticles, ligand-induced crystallization opens another pathway of making them photoactive. As a result, such materials can generate effectively the $HO^{\cdot}$ and $HOO^{\cdot}$ reactive oxygen species under the most intensive visible range of the solar radiation. This propensity may be beneficial for sewage water cleaning from organic pollutants [45, 46], but it is of concern for living

organisms welfare upon their adventitious intimate contact [47]. The ROS varieties generated within the cells of aquatic organisms upon exposure to such nanoparticles of the increased photoactivity make them potentially harmful in water media transparent to visible light [48]. The importance of thorough characterization of nanoparticles prior to bio-related testing is stressed by many researchers, but often not fully respected [25]. When seeking a predictive power, the nanotoxicity results obtained with limited data concerning the actual physicochemical status of the investigated nanomaterials are not appropriate for development of quantitative structure–activity relationship models. The revealed triple effect of complexation of titania nanomaterials with large organic molecules with acid properties, exemplified herein by rutin, consists of photosensitization, crystallization promotion and enhancement of the colloidal stability. It provides an original example of complex behavior of such systems, which needs to be considered for development of realistic scenarios of toxic action of titania (and other) nanoparticles in aqueous environments.

Conclusions

This study describes the complexation of a bioligand (rutin) at the surface of amorphous and crystalline ultrafine titanium dioxide particles, and elucidates the mechanism of ROS generation at the resultant hybrid nanomaterials. The EPR and fluorescence measurements using terephthalic acid as a chemical trap proved a successful photosensitization of TiO_2, and superoxide and hydroxyl radicals formation upon visible light irradiation. Photocurrent measurements confirmed a pronounce dioxygen and hydrogen peroxide influence on the interfacial charge transfer processes. The hydroxyl radical formation upon visible light irradiation is boosted in the presence of hydrogen peroxide, H_2O_2, which due to its redox properties can play a double role of a reactant prone to reduction and generation of hydroxyl radicals, and a redox agent destroying the intra-bandgap electronic states of the titania core. It was also revealed that binding of rutin leads not only to stable complexation of the surface titanium ions, but also promotes spontaneous crystallization of parent amorphous nanoparticles. This enhances their photoactivity and promotes an improved charge separation. As a result, a triple effect of complexation of titania nanomaterials with large organic molecules of acid properties, exemplified herein by rutin, was demonstrated. It consists of photosensitization, promotion of crystallization and enhancement of colloidal stability of ultrafine titania particles.

Acknowledgements This work was supported by the National Science Center within the SONATA (2016/21/D/NZ7/00611) project.

References

1. J. Schneider, M. Matsuoka, M. Takeuchi, J. Zhang, Y. Horiuchi, M. Anpo, D.W. Bahnemann, Chem Rev **114**, 9919 (2014)
2. A. Kubacka, M. Fernandez-Garcia, G. Colon, Chem Rev **112**, 1555 (2011)
3. O.-O. Prieto-Mahaney, N. Murakami, R. Abe, B. Ohtani, Chem Lett **38**, 238 (2009)
4. H. Kominami, K. Sumida, K. Yamamoto, N. Kondo, K. Hashimoto, Y. Kera, Res Chem Intermed **34**, 587 (2008)
5. Y.A. Attia, T.A. Altalhi, Res Chem Intermed **43**, 4051 (2017)
6. C. Ampelli, R. Passalacqua, C. Genovese, S. Perathoner, G. Centi, T. Montini, V. Gombac, J.J.D. Jaen, P. Fornasiero, RSC Adv **3**, 21776 (2013)
7. H. Taoda, Res Chem Intermed **34**, 417 (2008)
8. W. Iqbal, B. Tian, M. Anpo, J. Zhang, Res Chem Intermed **43**, 5187 (2017)
9. A. Weir, P. Westerhoff, L. Fabricius, K. Hristovski, N. Von Goetz, Environ Sci Technol **46**, 2242 (2012)
10. I.M. Hamouda, J Biomed Res **26**, 143 (2012)
11. D. Bharathi, V. Bhuvaneshwari, Res Chem Intermed **45**, 2065 (2019)
12. C. Botta, J. Labille, M. Auffan, D. Borschneck, H. Miche, M. Cabié, A. Masion, J. Rose, J.-Y. Bottero, Environ Pollut **159**, 1543 (2011)
13. B. Balraj, N. Senthilkumar, C. Siva, R. Krithikadevi, A. Julie, I.V. Potheher, M. Arulmozhi, Res Chem Intermed **43**, 2367 (2017)
14. N.S. Miyamoto, R. Miyamoto, E. Giamello, T. Kurisaki, H. Wakita, Res Chem Intermed **44**, 4577 (2018)
15. A. Elsaesser, C.V. Howard, Adv Drug Deliv Rev **64**, 129 (2012)
16. H. Kim, R. Manivannan, G. Heo, J. W. Ryu, Y.-A. Son, Res Chem Intermed **45**, 1 (2019)
17. K. Qi, F. Zasada, W. Piskorz, P. Indyka, J. Grybos, M. Trochowski, M. Buchalska, M. Kobielusz, W. Macyk, Z. Sojka, J Phys Chem C **120**, 5442 (2016)
18. A. Kozinska, A. Zadlo, P. Labuz, A. Broniec, P. Pabisz, T. Sarna, Photochem Photobiol **95**, 227 (2019)
19. Y. Zhang, Y. Chen, P. Westerhoff, K. Hristovski, J.C. Crittenden, Water Res **42**, 2204 (2008)
20. A.M. Khorasani, M. Goldberg, E.H. Doeven, G. Littlefair, J Biomater Tissue Eng **5**, 593 (2015)
21. P. Kocbek, K. Teskač, M.E. Kreft, J. Kristl, Small **6**, 1908 (2010)
22. G. Song, Y. Gao, H. Wu, W. Hou, C. Zhang, H. Ma, Environ Toxicol Chem **31**, 2147 (2012)
23. I. Iavicoli, V. Leso, A. Bergamaschi, J Nanomater **2012**, 5 (2012)
24. J. Chen, X. Dong, J. Zhao, G. Tang, J Appl Toxicol **29**, 330 (2009)
25. A. Menard, D. Drobne, A. Jemec, Environ Pollut **159**, 677 (2011)
26. J. Chen, X. Dong, Y. Xin, M. Zhao, Aquat Toxicol **101**, 493 (2011)
27. J.-J. Yin, J. Liu, M. Ehrenshaft, J.E. Roberts, P.P. Fu, R.P. Mason, B. Zhao, Toxicol Appl Pharmacol **263**, 81 (2012)
28. W.J. Cooper, R.G. Zika, Science **220**, 711 (1983)
29. E.-J. Park, J. Yi, K.-H. Chung, D.-Y. Ryu, J. Choi, K. Park, Toxicol Lett **180**, 222 (2008)
30. Y. Shi, F. Wang, J. He, S. Yadav, H. Wang, Toxicol Lett **196**, 21 (2010)
31. A. Kumar, A.K. Pandey, S.S. Singh, R. Shanker, A. Dhawan, Free Radic Biol Med **51**, 1872 (2011)
32. T. Hirakawa, Y. Nosaka, Langmuir **18**, 3247 (2002)
33. A.P. Gondikas, F. von der Kammer, R.B. Reed, S. Wagner, J.F. Ranville, T. Hofmann, Environ Sci Technol **48**, 5415 (2014)
34. Z. Hooresfand, S. Ghanbarzadeh, H. Hamishehkar, Pharm Sci **21**, 145 (2015)
35. K. Kataoka, N. Kijima, J. Akimoto, Inorg Chem **52**, 13861 (2013)
36. K. Kataoka, J. Akimoto, J Ceram Soc Jpn **124**, 710 (2016)
37. Y.V. Kolen'ko, K.A. Kovnir, A.I. Gavrilov, A.V. Garshev, J. Frantti, O.I. Lebedev, B.R. Churagulov, G. Van Tendeloo, M. Yoshimura, J Phys Chem B **110**, 4030 (2006)
38. M. Kitano, E. Wada, K. Nakajima, S. Hayashi, S. Miyazaki, H. Kobayashi, M. Hara, Chem Mater **25**, 385 (2013)
39. S.-H. Byeon, S.-O. Lee, H. Kim, J Solid State Chem **130**, 110 (1997)
40. A. Gajović, I. Friščić, M. Plodinec, D. Iveković, J Mol Struct **924**, 183 (2009)
41. E.L. Tae, S.H. Lee, J.K. Lee, S.S. Yoo, E.J. Kang, K.B. Yoon, J Phys Chem B **109**, 22513 (2005)
42. Y. Nosaka, A.Y. Nosaka, Chem Rev **117**, 11302 (2017)
43. M. Buchalska, P. Łabuz, Ł. Bujak, G. Szewczyk, T. Sarna, S. Maćkowski, W. Macyk, Dalton Trans **42**, 9468 (2013)

44. D.A. Armstrong, R.E. Huie, S. Lymar, W.H. Koppenol, G. Merényi, P. Neta, D.M. Stanbury, S. Steenken, P. Wardman, Bioinorg React Mech **9**, 59 (2013)
45. Q. Li, L. Wang, L. Zhang, H. Xie, Res Chem Intermed **45**, 757 (2019)
46. P. Verma, S.K. Samanta, Res Chem Intermed **43**, 6317 (2017)
47. S. Hall, T. Bradley, J.T. Moore, T. Kuykindall, L. Minella, Nanotoxicology **3**, 91 (2009)
48. K.T. Kim, S.J. Klaine, J. Cho, S.-H. Kim, S.D. Kim, Sci Total Environ **408**, 2268 (2010)

Affiliations

Przemysław Łabuz[1] · Joanna Gryboś[1] · Piotr Pietrzyk[1] · Kamila Sobańska[1] · Wojciech Macyk[1] · Zbigniew Sojka[1]

✉ Przemysław Łabuz
labuz@chemia.uj.edu.pl

[1] Faculty of Chemistry, Jagiellonian University, ul. Gronostajowa 2, 30-387 Kraków, Poland